nature physics

LETTERS

https://doi.org/10.1038/s41567-021-01421-x

Check for updates

OPEN

Thermodynamics of free and bound magnons in graphene

Andrew T. Pierce[1,5], Yonglong Xie[1,2,5], Seung Hwan Lee[1], Patrick R. Forrester[1], Di S. Wei[1], Kenji Watanabe[3], Takashi Taniguchi[4], Bertrand I. Halperin[1] and Amir Yacoby[1]✉

Symmetry-broken electronic phases support neutral collective excitations. For example, monolayer graphene in the quantum Hall regime hosts a nearly ideal ferromagnetic phase at specific filling factors that spontaneously breaks the spin-rotation symmetry[1–3]. This ferromagnet has been shown to support spin-wave excitations known as magnons that can be electrically generated and detected[4,5]. Although long-distance magnon propagation has been demonstrated via transport measurements, important thermodynamic properties of such magnon populations—including the magnon chemical potential and density—have not been measured. Here we present local measurements of electron compressibility under the influence of magnons, which reveal a reduction in the gap associated with the $\nu = 1$ quantum Hall state by up to 20%. Combining these measurements with the estimates of temperature, our analysis reveals that the injected magnons bind to electrons and holes to form skyrmions, and it enables the extraction of free magnon density, magnon chemical potential and average skyrmion spin. Our methods provide a means of probing the thermodynamic properties of charge-neutral excitations that are applicable to other symmetry-broken electronic phases.

The interplay between electron–electron interactions and isospin degeneracy in Landau levels can give rise to symmetry-broken states such as quantum Hall ferromagnets (QHFMs)[1,2]. The spin-polarized $\nu = 1$ state in monolayer graphene stands out due to its remarkable magnetic properties[3] and represents a unique platform for exploring charge-neutral spin excitations that may be useful for spintronics applications. Recent transport experiments have shown that voltage biases exceeding the Zeeman energy scale $E_Z = g\mu_B B$, where g is the electron g-factor and μ_B is the Bohr magneton, provide enough energy for electrons in the $\nu = 1$ edge channel to flip their spin and scatter out of the edge channel. This transition launches a magnonic excitation that may propagate through the bulk and produce a non-local voltage that can be detected micrometres away[4,5]. However, measurements of the thermodynamic properties of this magnon system—critical for harnessing these potentially useful charge-neutral excitations—remain outside the reach of both transport studies and conventional direct magnetic sensing owing to the dilute magnetization of the system. Here we perform local electronic compressibility measurements of the $\nu = 1$ QHFM with a scanning single-electron transistor (SET) and examine its response to the presence of magnons. We find that pumping magnons into the system results in a marked reduction in the charge gap, typically of about 15–20%. We argue that this gap reduction is a result of magnons binding with electrons or holes to form skyrmions, which, together with estimates of the temperature, allows us to determine the local magnon chemical potential and free magnon density in the system. The method of extracting the thermodynamic properties of magnons introduced in our experiments suggests novel routes towards realizing and probing Bose–Einstein condensation in QHFMs[6], and is more broadly applicable to other flat-band systems with spontaneously symmetry-broken states.

The device and measurement setup are shown in Fig. 1a,b. Figure 1c shows the two-terminal conductance G_{2T} between contacts 2 and 3 as a function of back-gate voltage V_{BG} and d.c. bias $V_{d.c.}$ at a magnetic field $B = 11$ T. Consistent with previous studies[4,5], for $-E_Z < V_{d.c.} < E_Z$, G_{2T} exhibits a plateau as a result of the quantization of the Hall conductance. However, the quantized Hall plateau disappears as soon as $|V_{d.c.}|$ reaches E_Z, signalling the onset of magnon generation and absorption processes.

To study the dependence of the $\nu = 1$ gap on the magnon population, we measure the electron chemical potential $\mu(\nu)$ as a function of filling factor ν at each value of $V_{d.c.}$ (Methods). Figure 1d shows two representative measurements of the electron chemical potential $\mu(\nu)$ near $\nu = 1$, with top-gate voltage $V_{TG} = 0$. The trace at $V_{d.c.} = 10$ mV (Fig. 1d, red curve) clearly exhibits a reduced gap compared with that at 0 mV (Fig. 1d, blue curve). Similar to the transport behaviour, the gap begins to principally change when $V_{d.c.}$ exceeds E_Z (Fig. 1e), initially dropping sharply and reaching suppression of about 20% at the highest biases investigated. The gap reduction shown in Fig. 1d,e, observed at many different locations (Extended Data Fig. 1), demonstrates the remarkable sensitivity of the $\nu = 1$ gap to the presence of magnons.

An important piece of evidence that the $\nu = 1$ gap suppression observed for d.c. biases $|V_{d.c.}| > E_Z$ results from magnon generation and absorption is its dependence on the local filling factor under the top gate, ν_{TG}. As a consequence of the spin order present in the region under the top gate, magnons freely propagate across when $\nu_{TG} = \pm 1$, but only weakly for $\nu_{TG} = 0$ and not at all for $\nu_{TG} = \pm 2$. Figure 2a shows the a.c. non-local voltage V_{NL} measured across contacts 5 and 6, normalized by the a.c. bias $V_{a.c.}$ applied between contacts 2 and 3. In addition to the vanishing non-local voltage for $|V_{d.c.}| < E_Z$, we find that for $|V_{d.c.}| > E_Z$, no appreciable signal is detected for $|\nu_{TG}| > 2$ or for $\nu_{TG} = 0$; on the other hand, a strong non-local voltage is observed for $0 < |\nu_{TG}| < 2$, in accordance with the expected transport characteristics and energy-splitting hierarchies shown in previous studies[4,5]. Next, we perform gap

[1]Department of Physics, Harvard University, Cambridge, MA, USA. [2]Department of Physics, Massachusetts Institute of Technology, Cambridge, MA, USA. [3]Research Center for Functional Materials, National Institute for Materials Science, Tsukuba, Japan. [4]International Center for Materials Nanoarchitectonics, National Institute for Materials Science, Tsukuba, Japan. [5]These authors contributed equally: Andrew T. Pierce, Yonglong Xie. ✉e-mail: yacoby@g.harvard.edu

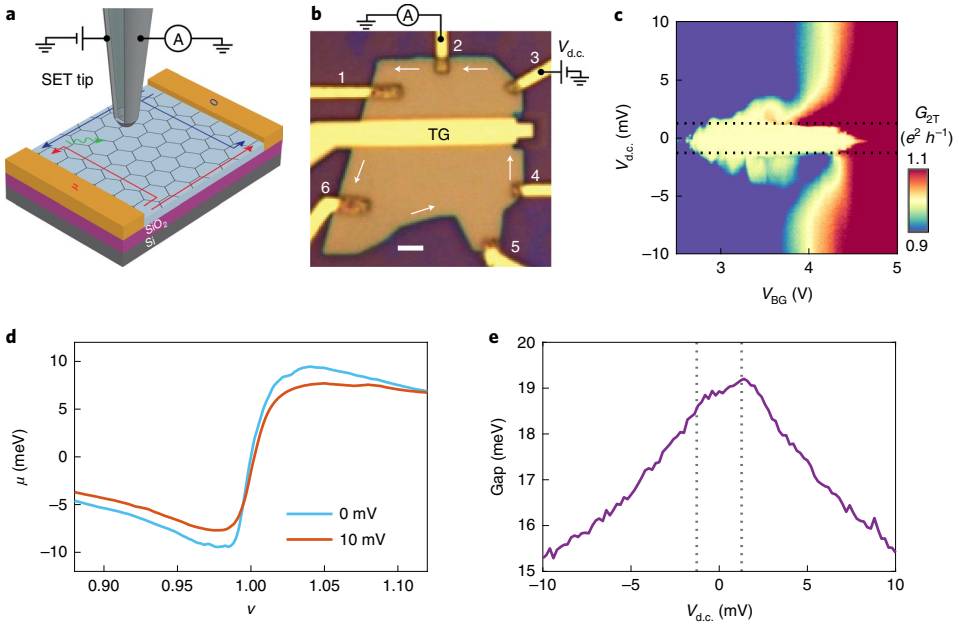

Fig. 1 | Device characterization and $\nu = 1$ sensitivity to magnons. a, Schematic of the experimental setup. The red and blue arrows denote the hot and cold quantum Hall edge states, respectively. The green curve denotes magnon generation for $\mu > E_Z$. **b**, Optical micrograph of the hBN-encapsulated monolayer graphene device. Scale bar, 2 µm. TG denotes the top gate. The white arrows indicate the chirality of the quantum Hall edge states. **c**, Two-terminal conductance G_{2T} near the $\nu = 1$ plateau measured at 11 T between contacts 2 and 3 with zero volts applied to the top gate. The plateau breaks down principally around $\pm E_Z$. **d**, The $\mu(\nu)$ measured at 11 T in the bulk near contact 5 at $V_{d.c.} = 0$ and 10 mV. The gap, taken as the peak excursion, is reduced in the case of $V_{d.c.} = 10$ mV. **e**, Bias-dependent energy gap extracted from the chemical potential measurements as in **d**. The gap begins to reduce near $\pm E_Z$ marked by the grey dotted lines.

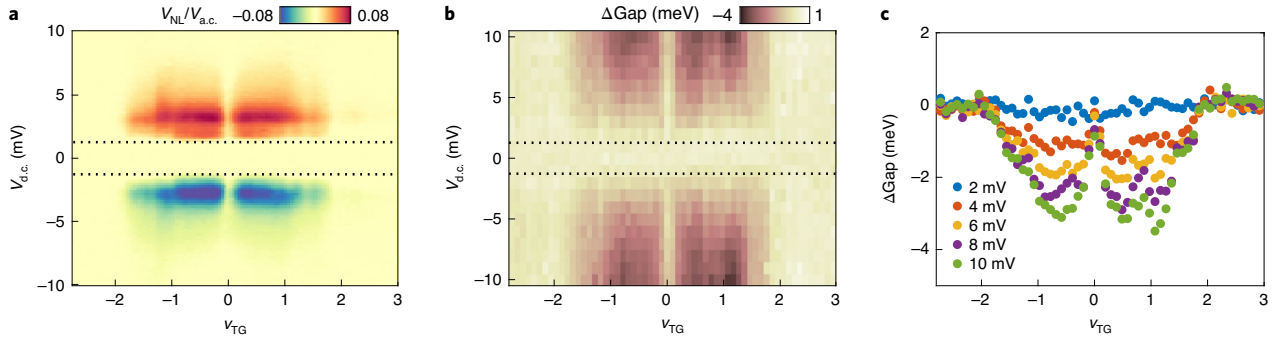

Fig. 2 | Non-local magnon transport and gap suppression. a, Non-local a.c. voltage V_{NL} measured between contacts 5 and 6 as a function of top-gate filling factor ν_{TG} and d.c. bias $V_{d.c.}$ applied across contacts 2 and 3. A non-local voltage appears near $\pm E_Z$ (black dotted lines) in accordance with the standard picture of magnon transport. **b**, Change in the measured $\nu = 1$ energy gap as a function of $V_{d.c.}$ and ν_{TG}. The value of ΔGap is calculated at each point by subtracting the average of the gap values at $|V_{d.c.}| < E_Z$. As in the case of V_{NL}, changes are only observed for $E_Z < |V_{d.c.}|$ and $0 < |\nu_{TG}| < 2$. **c**, Line traces from **b** showing the sharp disappearance of gap suppression near $\nu_{TG} = 0$.

measurements near contact 5 as a function of ν_{TG} and $V_{d.c.}$, using the same contacts for magnon generation. Figure 2b shows the reduction in gap at each $V_{d.c.}$, determined by subtracting—from each point—the average of the three traces with $|V_{d.c.}| < E_Z$ at each ν_{TG}, which is similar to the transport measurement (Fig. 2a); deviations in the $\nu = 1$ gap are only observed for $|V_{d.c.}| > E_Z$ and $0 < |\nu_{TG}| < 2$. Intriguingly, the bias dependence of the gap and behaviour of V_{NL} appear to define three regimes. First, biases $|V_{d.c.}| < E_Z$ result in no magnon generation and thus leave the gap intact. Second, for biases $E_Z < |V_{d.c.}| \lesssim 4E_Z$, the gap is rapidly suppressed and the magnitude of V_{NL} is large. Finally, for larger biases $|V_{d.c.}| \gtrsim 4E_Z$, the suppression is more gradual and the magnitude of V_{NL} is vanishingly small. These observations unambiguously establish that gap suppression results from magnon propagation into the bulk.

The first step toward understanding gap suppression is to identify the nature of charge excitation associated with the $\nu = 1$ gap in the absence of magnons. Theoretical studies[2,7–14] have proposed that the lowest-lying charged excitations at $\nu = 1$ are finite-sized skyrmions, consisting of a single charge $\pm e$ 'dressed' by one or more extra overturned spins or a valley texture. For skyrmions comprising flipped

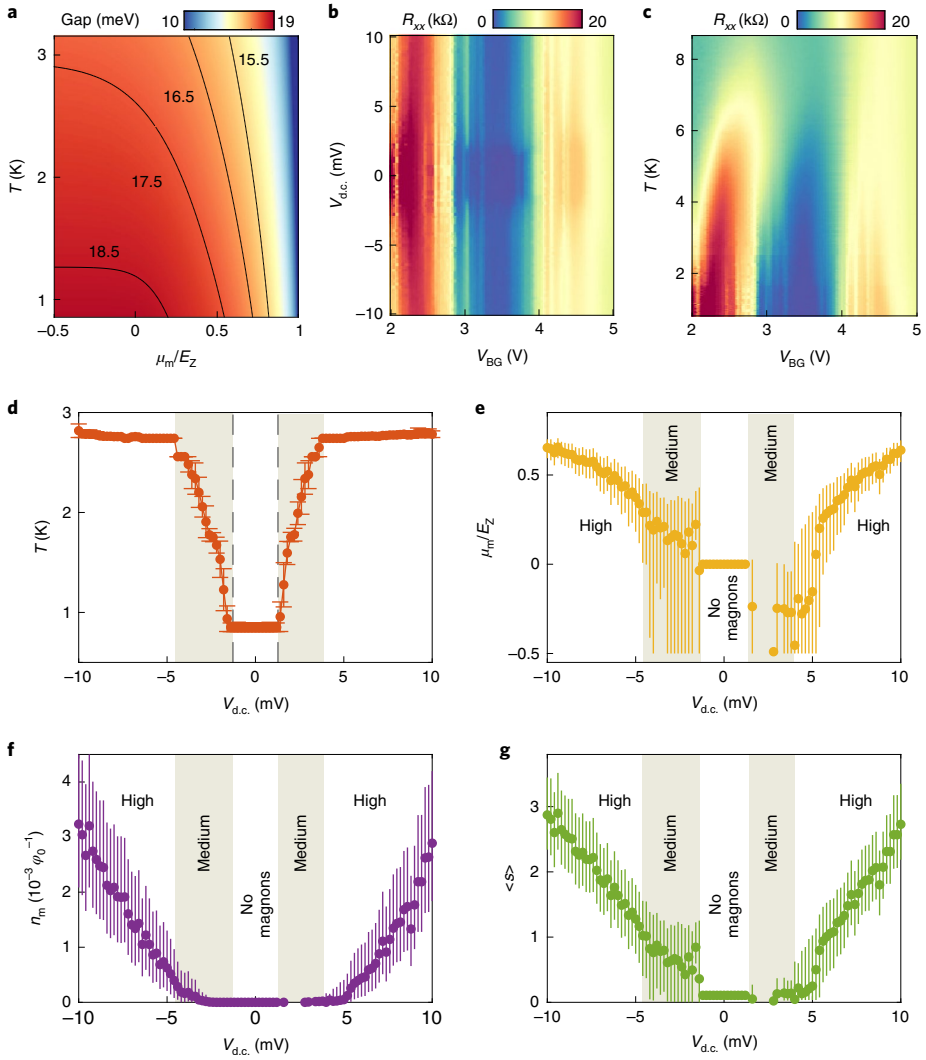

Fig. 3 | Thermodynamics of free and bound magnons. a, The $\nu=1$ gap as a function of magnon chemical potential μ_m/E_Z and temperature T computed using the skyrmion model. **b**, R_{xx} as a function of $V_{d.c.}$ applied to contact 3 near $\nu=1$ (Extended Data Fig. 3a shows the circuit). The centre of the $\nu=1$ plateau is around $V_{BG}=3.5$ V. **c**, R_{xx} as a function of temperature with no bias applied to contact 3 near $\nu=1$ using the same circuit as **b**. **d**, Temperature of the system as a function of $V_{d.c.}$ extracted from R_{xx} thermometry measurements (Methods). The grey dashed lines mark the Zeeman energy. **e**–**g**, Magnon chemical potential μ_m/E_Z (**e**), free magnon density per flux n_m (**f**) and the number of extra flipped spins carried by charge $<s>$ (**g**) extracted from the skyrmion model (Methods). The shaded region corresponds to a medium-bias regime where heating due to magnon injection plays a key role.

spins (referred to as 'spin skyrmions'), the excitation energy is determined by the competition between E_Z and exchange energy. We, therefore, consider a phenomenological model of spin skyrmions with s flipped spins[15], whose occupation follows a Boltzmann distribution (Methods and Supplementary Information). Extended Data Fig. 2 shows the best fits to the data using this phenomenological model. The satisfactory agreement between the fit and data at many different locations validates our model and allows us to determine the Coulomb energy E_C, which sets the overall scale for the skyrmion and magnon energies (Methods), which is around 21.4 meV, consistent with previous local compressibility measurements of the $\nu=-1$ gap[11]. Most notably, we find that $<s>$, the mean number of extra spins carried by a charge excitation, is less than 6% of an electron spin in the absence of injected magnons, establishing that the lowest-lying charge excitation consists of bare electrons and holes.

The observed gap suppression can be naturally captured by extending the phenomenological spin skyrmion model to incorporate the presence of magnons[16] (Methods), where we describe the magnons by an effective Bose–Einstein distribution with chemical potential μ_m (refs. [17,18]) and electron temperature T. The magnon chemical potential μ_m defines an equilibrium between free magnons and those bound as flipped spins in skyrmions, and may be non-zero due to S_Z conservation (that is, magnon number conservation) in the bulk, which results from the weak spin–orbit coupling and small number of nuclear spins present in graphene. Since each magnon represents one flipped spin and therefore one unit of E_Z, pumping magnons into the system amounts to externally supplying some of the work needed to flip spins. Assuming there is equilibration between the charge excitations and free magnons (Methods), this results in a reduction in the Zeeman free-energy cost by μ_m

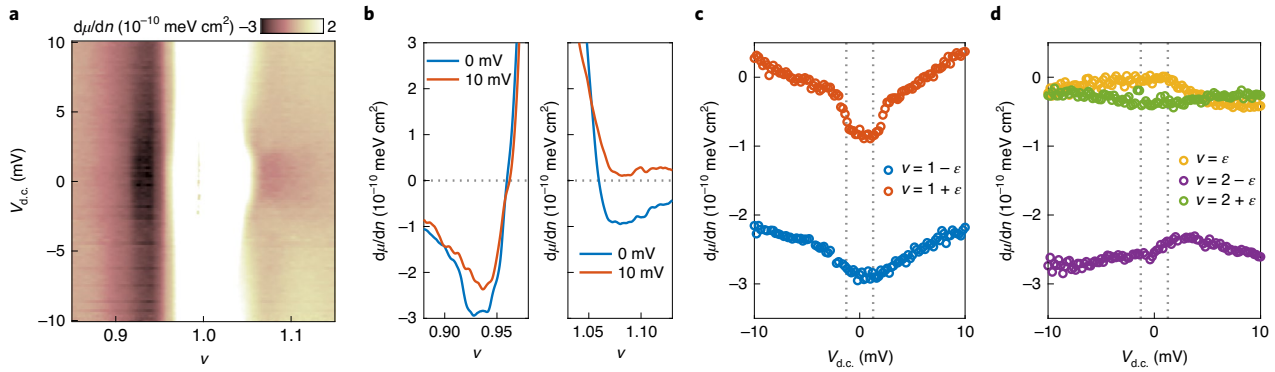

Fig. 4 | Suppression of negative compressibility by the presence of magnons. a, The values of dμ/dn near $\nu = 1$ measured as a function of $V_{d.c.}$. **b**, Representative dμ/dn traces on the hole (left) and electron (right) sides of $\nu = 1$ measured with $V_{d.c.} = 0$ mV (blue) and $V_{d.c.} = 10$ mV (red), showing that the negative compressible states are suppressed by the presence of magnons. **c**, Averaged dμ/dn on the hole (blue) and electron (red) sides of $\nu = 1$ as a function of $V_{d.c.}$. The grey dotted lines mark the Zeeman energy $\pm E_Z$. **d**, Average dμ/dn on the other Wigner crystal states as a function of d.c. bias, showing no suppression by $V_{d.c.}$. The grey dotted lines mark the Zeeman energy $\pm E_Z$.

per flipped spin for the spin skyrmion, favouring the formation of skyrmions over bare electrons or holes and thus suppressing the overall charge gap. To compare the predictions of this model with our experiments, we compute the $\nu = 1$ gap as a function of μ_m and T with the parameters obtained by fitting the measured zero-bias $\mu(\nu)$ curves (Fig. 3a and Methods). The results of these calculations indicate that considerable enhancements of μ_m and T are required to achieve the measured gap suppression at large biases (as shown by the constant-gap contours in Fig. 3a).

To use our model to extract the magnon chemical potential μ_m, an independent estimate of electron temperature T as a function of d.c. bias is required. Such an estimate is furnished by a measurement of longitudinal resistance R_{xx} in the presence of magnon pumping using a circuit configuration that is insensitive to magnon absorption at the contacts (Methods). Strikingly, we find that the measured R_{xx} displays a sudden increase for $|V_{d.c.}| > E_Z$, indicative of its magnon origin. The comparison of the bias-dependent R_{xx} measurement with the measurement of R_{xx} at zero bias as a function of temperature (Fig. 3c) suggests that injecting magnons into the system results in the electron temperature heating up to approximately 3 K. By finding the best-fit temperature for each $V_{d.c.}$, we extract the quantitative values of electron temperature T (Fig. 3d), which spans three distinct regimes. In the low-bias regime of $|V_{d.c.}| < E_Z$, no magnons are generated and T remains at the base temperature. Between E_Z and approximately $4E_Z$, T rapidly increases as a function of bias. Finally, above approximately $4E_Z$, T saturates and once again remains constant to the highest biases investigated. We have performed similar estimates using a variety of circuit configurations, both two- and four-terminal configurations (Extended Data Figs. 3–5), which point to a similar range of temperatures.

Estimates of $T(V_{d.c.})$ and the results of our model calculations allow us to relate the measured gap values to μ_m. Specifically, we determine $\mu_m(V_{d.c.})$ (Fig. 3e) by matching our measured gap values and T to the simulation results (Fig. 3a,d; Extended Data Fig. 6 provides the analysis at another location). As in the case of T, the measured gap and V_{NL}, we find that $\mu_m(V_{d.c.})$ exhibits three separate regimes. At low bias, that is, $|V_{d.c.}| < E_Z$, we have $\mu_m = 0$ in accordance with the general properties of the Bose–Einstein distribution. At intermediate bias, namely, $E_Z < |V_{d.c.}| \lesssim 4E_Z$, we observe no increase in μ_m, despite the presence of magnon transport signatures in V_{NL} (Extended Data Fig. 7). Thus, the behaviour of the measured gap in the intermediate-bias regime can be explained as a result of heating due to the injected magnons without invoking the possibility of skyrmion formation. At high bias, that is, $4E_Z \lesssim |V_{d.c.}|$, where T is approximately 3 K, we extract the values of μ_m in excess of zero, as expected in the presence of magnon pumping. We emphasize that gap suppression observed in this regime cannot be explained by heating alone, as this would require the temperature to continue to linearly increase beyond $V_{d.c.} = \pm 5$ mV and reach as high as 6 K at $V_{d.c.} = \pm 10$ mV, in direct contradiction to the temperature estimated from our zero-bias R_{xx} measurements (Fig. 3b,c and Extended Data Fig. 3).

A further insight can be gained by examining the density n_m of the equilibrated free magnons obtained from our calculations and the mean number of overturned spins per skyrmion $\langle s \rangle$ as a function of $V_{d.c.}$. Figure 3f shows the extracted $n_m(V_{d.c.})$ in units of magnons per flux quantum ϕ_0. In the range of $E_Z < |V_{d.c.}| \lesssim 4E_Z$, the finite V_{NL} and gap suppression measurements demonstrate that magnons are at work (Extended Data Fig. 7). However, we find that μ_m does not increase in this range and n_m, therefore, remains negligibly small. We speculate that two possible scenarios may explain this apparent contradiction. One hypothesis is that for $E_Z < |V_{d.c.}| \lesssim 4E_Z$, there is an additional population of magnons, possibly of a very long wavelength, which is not in thermal equilibrium with the electrons and thus is not captured in the computed n_m values despite contributing to G_{2T} and V_{NL}. A comparison of the lower bound on the magnon lifetime obtained from our transport measurements and device geometry with theoretical estimates of the magnon–electron scattering time shows that magnons with k less than approximately $0.01 l_B^{-1}$, where l_B is the magnetic length, may scatter with skyrmions slowly enough to fail to equilibrate. A second, more exotic possibility is that, in fact, only a very small number of magnons are present in this bias regime, which would imply that a highly efficient mechanism of transport is responsible for the changes in G_{2T} and V_{NL}. On the other hand, for $4E_Z \lesssim |V_{d.c.}|$, a finite population of equilibrated free magnons emerges, which appears to linearly scale with $V_{d.c.}$. We note that for a 100 μm^2 sample at 11 T, the highest equilibrium magnon density of about 3×10^{-3} per ϕ_0 corresponds to a total number of equilibrated magnons only of the order of 300. It is possible that a population of non-equilibrated magnons also persists in this regime. In any case, these observations suggest that the absorption rate of magnons at the contacts may be outpaced by the finite population of free magnons, causing V_{NL} to weaken and G_{2T} to level off at high biases (Extended Data Fig. 7). Finally, the corresponding $\langle s \rangle$ (Fig. 3g) displays a similar trend as n_m and is three excess overturned spins at the highest biases, consistent with our overall mechanism of gap suppression. The change in behaviour as $V_{d.c.}$ exceeds $4E_Z$ may be related to the large increase in

specific heat as μ_m increases (Supplementary Information) and/or to higher-energy valley–spin excitations hosted by a valley-polarized charge-density-wave ground state (Methods)[19].

In a low-density electron system, correlation effects induced by the Coulomb repulsion between carriers can result in negative (inverse) electronic compressibility $d\mu/dn$ (refs. [20,21]), which can be observed at $\nu = 0 + \varepsilon$, $1 \pm \varepsilon$ and $2 \pm \varepsilon$ (Fig. 4a,b). The associated correlation energy scale, approximated in our model to the leading order by $E_{WC} \sim \sqrt{\varepsilon}$, governs the magnitude of negative compressibility. Intriguingly, we find that the negative-compressibility features at $\nu = 1 \pm \varepsilon$ respond differently to $V_{d.c.}$ than those at $\nu = 0 + \varepsilon$ and $2 \pm \varepsilon$, with those at $\nu = 1 \pm \varepsilon$ being greatly diminished at high bias voltages. The pronounced reduction with increasing bias for $E_Z < |V_{d.c.}| \lesssim 4E_Z$ is presumably due to heating, but the reduction with increasing bias beyond this point—where the electron temperature is found to be constant—signals that the strength of correlations is suppressed by the presence of magnons. A possible explanation is that the formation of skyrmions may decrease the magnitude of correlation energy, because the electric charge of a skyrmion is more spread out than a bare electron or hole in the lowest Landau level. A comparison of the average negative compressibility for $\nu = 0 + \varepsilon$, $1 \pm \varepsilon$ and $2 \pm \varepsilon$ (Fig. 4c,d) shows that it is sensitive to $V_{d.c.}$ only near $\nu = 1$, providing additional evidence for the magnon origin. Further study is required to fully establish the microscopic mechanism of these effects.

Looking ahead, the methods of measuring μ_m demonstrated here can be used to map out this important quantity over extended spatial regions. As the gradient of μ_m is the driving force of magnon currents, such studies may provide further new insights into the nature of magnon transport in the system[22], including the $\nu = 0$ state in monolayer graphene, which may support spin superfluidity[6,23]. The ability to tune μ_m in situ raises the possibility of dynamical control of quantum phases analogous to recent pump–probe experiments[24], but using magnetic excitations instead of terahertz frequencies. Finally, our combined ability of manipulating and probing the magnon chemical potential is immediately applicable to intriguing correlated insulating states recently reported in moiré superlattice systems, which are expected to support electrically addressable neutral excitations similar to the $\nu = 1$ QHFM[25–27].

Online content

Any methods, additional references, Nature Research reporting summaries, source data, extended data, supplementary information, acknowledgements, peer review information; details of author contributions and competing interests; and statements of data and code availability are available at https://doi.org/10.1038/s41567-021-01421-x.

Received: 17 February 2021; Accepted: 15 October 2021;
Published online: 13 December 2021

References

1. Nomura, K. & MacDonald, A. H. Quantum Hall ferromagnetism in graphene. *Phys. Rev. Lett.* **96**, 256602 (2006).
2. Girvin, S. M. in *Topological Aspects of Low Dimensional Systems* (eds Comtet, A. et al.) 53–175 (Springer, 1999).
3. Young, A. F. et al. Spin and valley quantum Hall ferromagnetism in graphene. *Nat. Phys.* **8**, 550–556 (2012).
4. Wei, D. S. et al. Electrical generation and detection of spin waves in a quantum Hall ferromagnet. *Science* **362**, 229–233 (2018).
5. Zhou, H., Polshyn, H., Taniguchi, T., Watanabe, K. & Young, A. F. Solids of quantum Hall skyrmions in graphene. *Nat. Phys.* **16**, 154–158 (2020).
6. Takei, S., Yacoby, A., Halperin, B. I. & Tserkovnyak, Y. Spin superfluidity in the $\nu = 0$ quantum Hall state of graphene. *Phys. Rev. Lett.* **116**, 216801 (2016).
7. Sondhi, S. L., Karlhede, A., Kivelson, S. A. & Rezayi, E. H. Skyrmions and the crossover from the integer to fractional quantum Hall effect at small Zeeman energies. *Phys. Rev. B* **47**, 16419–16426 (1993).
8. Fertig, H. A., Brey, L., Côté, R. & MacDonald, A. H. Charged spin-texture excitations and the Hartree-Fock approximation in the quantum Hall effect. *Phys. Rev. B* **50**, 11018–11021 (1994).
9. Fertig, H. A. et al. Hartree-Fock theory of skyrmions in quantum Hall ferromagnets. *Phys. Rev. B* **55**, 10671–10680 (1997).
10. Alicea, J. & Fisher, M. P. A. Graphene integer quantum Hall effect in the ferromagnetic and paramagnetic regimes. *Phys. Rev. B* **74**, 075422 (2006).
11. Abanin, D. A., Feldman, B. E., Yacoby, A. & Halperin, B. I. Fractional and integer quantum Hall effects in the zeroth Landau level in graphene. *Phys. Rev. B* **88**, 115407 (2013).
12. Yang, K., Das Sarma, S. & MacDonald, A. H. Collective modes and skyrmion excitations in graphene SU(4) quantum Hall ferromagnets. *Phys. Rev. B* **74**, 075423 (2006).
13. Lian, Y., Rosch, A. & Goerbig, M. O. SU(4) skyrmions in the $\nu = \pm 1$ quantum Hall state of graphene. *Phys. Rev. Lett.* **117**, 056806 (2016).
14. Lian, Y. & Goerbig, M. O. Spin-valley skyrmions in graphene at filling factor $\nu = -1$. *Phys. Rev. B* **95**, 245428 (2017).
15. Wójs, A. & Quinn, J. J. Spin excitation spectra of integral and fractional quantum Hall systems. *Phys. Rev. B* **66**, 045323 (2002).
16. Kallin, C. & Halperin, B. I. Excitations from a filled Landau level in the two-dimensional electron gas. *Phys. Rev. B* **30**, 5655–5668 (1984).
17. Demokritov, S. O. et al. Bose–Einstein condensation of quasi-equilibrium magnons at room temperature under pumping. *Nature* **443**, 430–433 (2006).
18. Du, C. et al. Control and local measurement of the spin chemical potential in a magnetic insulator. *Science* **357**, 195–198 (2017).
19. Atteia, J. & Goerbig, M. O. SU(4) spin waves in the $\nu = \pm 1$ quantum Hall ferromagnet in graphene. *Phys. Rev. B* **103**, 195413 (2021).
20. Eisenstein, J. P., Pfeiffer, L. N. & West, K. W. Negative compressibility of interacting two-dimensional electron and quasiparticle gases. *Phys. Rev. Lett.* **68**, 674–677 (1992).
21. Eisenstein, J. P., Pfeiffer, L. N. & West, K. W. Compressibility of the two-dimensional electron gas: measurements of the zero-field exchange energy and fractional quantum Hall gap. *Phys. Rev. B* **50**, 1760–1778 (1994).
22. Wei, N., Huang, C. & MacDonald, A. H. Scattering of magnons at graphene quantum-Hall-magnet junctions. *Phys. Rev. Lett.* **126**, 117203 (2020).
23. Stepanov, P. et al. Long-distance spin transport through a graphene quantum Hall antiferromagnet. *Nat. Phys.* **14**, 907–911 (2018).
24. Fausti, D. et al. Light-induced superconductivity in a stripe-ordered cuprate. *Science* **331**, 189–191 (2011).
25. Bernevig, B. A. et al. TBG V: exact analytic many-body excitations in twisted bilayer graphene Coulomb Hamiltonians: charge gap, Goldstone modes and absence of Cooper pairing. *Phys. Rev. B* **103**, 205415 (2020).
26. Kumar, A., Xie, M. & MacDonald, A. H. Lattice collective modes from a continuum model of magic-angle twisted bilayer graphene. *Phys. Rev. B* **104**, 035119 (2021).
27. Khalaf, E., Bultinck, N., Vishwanath, A. & Zaletel, M. P. Soft modes in magic angle twisted bilayer graphene. Preprint at https://arxiv.org/abs/2009.14827 (2020).

Methods

Sample preparation. The device consists of monolayer graphene encapsulated by two layers of hexagonal boron nitride (hBN) on a p-doped Si substrate with a 285 nm layer of SiO_2, and was fabricated using a dry transfer technique. A gold top gate was defined using electron-beam lithography and thermally evaporated Cr/Au. The final device geometry was defined by electron-beam lithography and reactive-ion etching. Edge contacts were made by thermally evaporating Cr/Au while rotating the sample using a tilted rotation stage.

Measurements. All the measurements were carried out in a ^{3}He cryostat with a base temperature of approximately 500 mK. The transport measurements were performed using standard lock-in techniques with a 100 μV excitation with frequencies ranging from 17 to 40 Hz. The temperature-dependent measurements were recorded by applying current to a resistive heater located at the ^{3}He stage. The SET tips were fabricated using the procedure described elsewhere[28]. The diameter of the SET is approximately 100 nm, and it was held about 300 nm above the encapsulated graphene. Compressibility measurements were performed using d.c. and a.c. techniques similar to those described elsewhere[28]. The SET serves as a sensitive detector of changes in electrostatic potential $\delta\varphi$, which is related to the chemical potential of the graphene flake by $\delta\mu = -e\delta\varphi$ when the system is in equilibrium. In the a.c. scheme used to measure $\mathrm{d}\mu/\mathrm{d}n$, an a.c. voltage is applied to the Si back gate to weakly modulate the carrier density of graphene, and the corresponding changes in SET current are converted to chemical potential by normalizing the signal by that from a small a.c. bias directly applied to the sample. For d.c. measurements, an analogue proportional–integral–derivative controller is used to maintain the SET current at a fixed value by changing the tip–sample bias. The corresponding change in sample voltage provides a direct measure of $\mu(n)$.

Spin skyrmion model. We briefly summarize the skyrmion model used for estimating the magnon chemical potential μ_m. Assuming that both density of overturned spins and deviation from $\nu = 1$ is small, the densities of electron-like and hole-like skyrmions with s overturned spins, denoted as n_s^e and n_s^h, respectively, follow the Boltzmann distributions given by

$$n_s^e = e^{-(E_s^e - s\mu_m - \mu + a_e\delta\mu_{WC}(\nu))/T},$$

$$n_s^h = e^{-(E_s^h - s\mu_m + \mu + a_h\delta\mu_{WC}(\nu))/T}$$

where E_s^e and E_s^h are the energy of elementary charged electron-like and hole-like excitations at $\nu = 1$, respectively; μ is the electron chemical potential; T is the temperature; $\delta\mu_{WC}(\nu)$ is a Wigner crystal-like energy functional; a_e and a_h are fit parameters; and μ_m is the magnon chemical potential (Supplementary Information provides complete details of the parameters used). The energies E_s^e and E_s^h as well as $\delta\mu_{WC}(\nu)$ are parametrized by an overall phenomenological Coulomb energy scale E_C that is treated as a fit parameter to be obtained by fitting the zero-bias μ traces. Extended Data Fig. 2 shows examples of the zero-bias fit results, which are in excellent agreement with the experimental traces, along with the fit parameters E_C, a_e, a_h and a Gaussian density-broadening parameter $\Delta\nu$. These fit parameters, along with our independent measurements of the $\nu = 1$ gap and T, can then be combined with the distributions n_s^e and n_s^h to determine μ_m and other thermodynamic properties (Fig. 3e–g, Extended Data Fig. 6b–d and Supplementary Information).

***R*$_{xx}$ and *G*$_{2T}$ thermometry.** To obtain an estimate of the electron temperature T independent of our compressibility measurements, we perform R_{xx} measurements in the presence of magnon generation using the circuit shown in Extended Data Fig. 3. Keeping contact 2 grounded, we apply an a.c. bias between contacts 1 and 4 and measure the longitudinal a.c. voltage V_{xx} across contacts 5 and 6. We emphasize that this measurement of R_{xx} is different than the non-local voltage and is not expected to be directly sensitive to contributions from magnon generation and absorption, and we expect the phonon contribution to R_{xx} to be small in the temperature range of interest (Supplementary Information provides further details). To generate magnons, a d.c. bias is applied to contact 3; in this case, no a.c. modulation is applied to the magnon generation contacts. Strikingly, the measured R_{xx} as a function of d.c. bias (Extended Data Fig. 3) displays an abrupt change when the applied d.c. bias exceeds the Zeeman energy, reminiscent of the response observed in the magnon transport experiments with a.c. modulation applied to contact 3 (Fig. 1). However, we emphasize that the change in R_{xx} is not caused by magnon absorption events as in the case of the V_{NL} signal discussed earlier or by other hot-carrier effects, because the a.c. modulation used for monitoring R_{xx} is not applied to the d.c.-biased contacts used for magnon generation. Extended Data Fig. 3d,e shows R_{xx} measured using the same circuit with no d.c. bias applied to contact 3 as a function of temperature. Under these conditions, the electron temperature is expected to be well equilibrated with the lattice temperature[29]. Remarkably, we find good agreement between an R_{xx} trace measured at a given d.c. bias and that at a given temperature (Fig. 3e, where the error bar is estimated by matching the R_{xx} value with a d.c. bias to the temperature-dependent R_{xx} with up to 5% error), suggesting that the change in R_{xx} at a d.c. bias greater than the Zeeman energy is equivalent to an increase in the temperature of the system. We note that although the phonon temperature is expected to remain near the base temperature in the biased case, we do not expect phonons to play an important role in our measurements (Supplementary Information). A comparison of these two R_{xx} measurements, therefore, allows us to determine the temperature of the system when magnons are pumped into the system and uniquely determine μ_m.

Alternatively, the two-terminal conductance G_{2T} may be used as a proxy for the temperature instead of the four-terminal R_{xx}. Extended Data Fig. 4a,b shows the bias- and temperature-dependent two-terminal conductance G_{2T}, respectively, measured with an a.c. voltage between contacts 1 and 4 using the circuit shown in Extended Data Fig. 3a. As in the case of R_{xx} measurements, once the system has heated beyond about 5 K, the principal signatures of the quantum Hall effect vanish (in this case, the plateau), thus placing an overestimated but crucial upper bound for the temperature of our system. Extended Data Fig. 4c shows G_{2T} at a d.c. bias of –10 mV compared with a selection of zero-bias traces taken at various temperatures, which points to a temperature of about 3 K—in good agreement with the results obtained by analysing R_{xx}. We have verified this behaviour in numerous circuit configurations—both two-terminal and four-terminal configurations—which consistently point to the same range of temperatures (Extended Data Fig. 5, except for the positive biases shown in Extended Data Fig. 5h, which is likely due to a bad contact). We regard the R_{xx} measurements as a more reliable indicator of temperature, as G_{2T} is more susceptible to effects stemming from the contact resistance. Nevertheless, our observation that both R_{xx} and G_{2T} thermometry techniques yield approximately the same electron temperature leads us to conclude that reliable estimates can be derived from either technique.

Thermalization of magnons and electrons. To understand the degree of equilibration between the skyrmions and free magnons and why there could be an additional population of magnons that are not in equilibrium with the electrons, we note that the degree of thermalization between a magnon and the skyrmion population depends on its momentum k. Moderate-to-short-wavelength magnons with $k \gtrsim l_B^{-1}$ are equivalent to well-separated electron–hole pairs and therefore may be expected to thermalize with the skyrmion population very quickly—at a rate nearly equal to that of a single free electron or hole. On the other hand, long-wavelength magnons with momenta $k \ll l_B^{-1}$ are equivalent to tightly bound electron–hole pairs, which only carry a small electric dipole moment and therefore are expected to couple more weakly to skyrmions and thermalize more slowly. In general, for a given magnon to equilibrate with the skyrmion population, its lifetime must exceed the mean magnon–electron scattering time $\tau_{me}(k)$. The magnon–electron scattering rate $\Gamma_k = \tau_{me}^{-1}$ has been calculated within the context of bilayer QHFMs to be[30]

$$\Gamma_k = \delta\nu \frac{E_C^2 k^3 l_B^4}{\hbar^2 v(k)}$$

where $\delta\nu$ is the difference in the Landau-level filling factor from the nearest integer (taken as 0.01 here) and $v(k)$ is the magnon velocity. To obtain a lower bound for the magnon lifetime, we note that in the absence of magnetic impurities, we expect magnon absorption events at the contacts[4] to be the dominant mechanism by which magnons are removed from the bulk. The requirement that magnons survive long enough to travel the approximately 10 μm distance between the contacts in the device, therefore, allows us to estimate a lower bound on the lifetime $\tau_{min} \approx d/v(k)$, where $d = 10$ μm. Extended Data Fig. 8 plots the two timescales $\tau_{me}(k)$ and $\tau_{min}(k)$ as a function of k, and shows that only very-long-wavelength magnons with $k \lesssim 0.01 l_B^{-1}$ are expected to scatter slowly enough with skyrmions to fail to come into equilibrium.

Role of valley skyrmions. A number of theoretical studies have considered the nature of the lowest-lying charged excitations in the $\nu = 1$ QHFM[10–14]. Although valley skyrmions may be favoured under ideal conditions, the presence of a boron nitride substrate in encapsulated devices may result in the breaking of sublattice symmetry and therefore disfavour the formation of valley skyrmions. Although we do not find direct evidence for a gap at the charge-neutrality point (CNP) in our device, we observe a robust incompressible state at $\nu = 5/3$, with an incompressible peak comparable in magnitude to those occurring at $\nu = 1/3$ and 2/3 (Extended Data Fig. 9). The conspicuous absence of this state in previous local compressibility measurements on suspended devices was attributed to low-lying valley-skyrmionic excitations with energy less than that of a Laughlin quasiparticle[11,28]. Thus, the observation of robust incompressible states at $\nu = 5/3$ strongly suggests that valley skyrmions are disfavoured in our sample. Furthermore, within the spin skyrmion model of gap suppression, we do not expect the presence of magnons to alter the energy cost of adding a valley skyrmion. These conclusions also hold for valley-coherent ground states, in which the spin excitation spectrum is expected to be the same as the valley-polarized case considered above[19]. Hence, we conclude that valley skyrmions are unlikely to play an important role in the observed $\nu = 1$ gap reduction.

Discussion of a possible gap at the CNP. To search for evidence of sublattice symmetry breaking, we performed high-resolution local compressibility measurements near the CNP at zero magnetic field, which was compared with a

model that considers the sublattice-gapped Dirac form $\mu(n) = \sqrt{\frac{\Delta_0^2}{4} + \frac{\pi\hbar^2 n}{\hbar^2}}$, where Δ_0 and ν_F are the sublattice gap and Fermi velocity, respectively, and $\hbar$ is the reduced Planck constant. Extended Data Fig. 10 shows two fits of the measured inverse compressibility at zero magnetic field to the sublattice-gapped Dirac model, one with disorder broadening and the other one without broadening. The unbroadened fit favours a scenario in which the sublattice gap is zero. The broadened fit, however, yields a mean squared error approximately one-half that of the unbroadened fit, as well as favours a scenario in which the sublattice gap is approximately 12.3 meV with a broadening of $7\times10^9\,\mathrm{cm}^{-2}$, consistent with that extracted from our fit to the $\nu=1$ gap at a high magnetic field. These considerations suggest that sublattice symmetry is likely broken by the boron nitride substrate, disfavouring the formation of valley skyrmions, despite the compressibility signature of the gap being obscured by disorder broadening at zero magnetic field.

Data availability

Source data are provided with this paper. All other data that support the findings of this paper are available from the corresponding author upon reasonable request.

Code availability

The code that supports the findings of this study is available from the corresponding author upon reasonable request.

References

28. Feldman, B. E., Krauss, B., Smet, J. H. & Yacoby, A. Unconventional sequence of fractional quantum Hall states in suspended graphene. *Science* **337**, 1196–1199 (2012).
29. Fong, K. C. et al. Measurement of the electronic thermal conductance channels and heat capacity of graphene at low temperature. *Phys. Rev. X* **3**, 041008 (2013).
30. Green, A. G. & Cooper, N. R. Dissipative transport in quantum Hall ferromagnets by spin-wave scattering. *Phys. Rev. B* **65**, 125329 (2002).

Acknowledgements

We acknowledge discussion with P. Jarillo-Herrero and P. Wang. This work was primarily supported by the US Department of Energy, Basic Energy Sciences Office, Division of Materials Sciences and Engineering, under award DE-SC0001819. Fabrication of samples was supported by the US Department of Energy, Basic Energy Sciences Office, Division of Materials Sciences and Engineering, under award DE-SC0019300. A.Y. also acknowledges the Gordon and Betty Moore Foundations EPiQS Initiative through grant no. GBMF9468; ARO grant no. W911NF-14-1-0247; and the STC Center for Integrated Quantum Materials, National Science Foundation (NSF), grant no. DMR-1231319. A.T.P. acknowledges support from the Department of Defense through the National Defense Science and Engineering Graduate Fellowship (NDSEG) program. Y.X. acknowledges partial support from the Harvard Quantum Initiative in Science and Engineering. A.T.P., Y.X. and A.Y. acknowledge support from the Harvard Quantum Initiative Seed Fund. P.R.F. acknowledges support from the NSF Graduate Research Fellowship under grant no. DGE 1745303. K.W. and T.T. acknowledge support from the Elemental Strategy Initiative conducted by the MEXT, Japan, grant no. JPMXP0112101001; JSPS KAKENHI grant no. JP20H00354; and the CREST (JPMJCR15F3), JST. This work was performed, in part, at the Center for Nanoscale Systems (CNS), a member of the National Nanotechnology Infrastructure Network, which is supported by the NSF under award no. ECS-0335765. CNS is part of Harvard University.

Author contributions

A.T.P., Y.X. and A.Y. designed the experiment. A.T.P. and Y.X. performed the scanning SET experiment and temperature-dependent transport measurements and they analysed the data with input from A.Y. S.H.L. fabricated the device and performed the transport measurements using the dilution refrigerator. B.I.H., A.T.P. and Y.X. performed the theoretical analysis and carried out the numerical calculations. K.W. and T.T. provided the hBN crystals. All the authors participated in discussions and in writing of the manuscript.

Competing interests

The authors declare no competing interests.

Additional information

Extended data is available for this paper at https://doi.org/10.1038/s41567-021-01421-x.

Supplementary information The online version contains supplementary material available at https://doi.org/10.1038/s41567-021-01421-x.

Correspondence and requests for materials should be addressed to Amir Yacoby.

Peer review information *Nature Physics* thanks the anonymous reviewers for their contribution to the peer review of this work

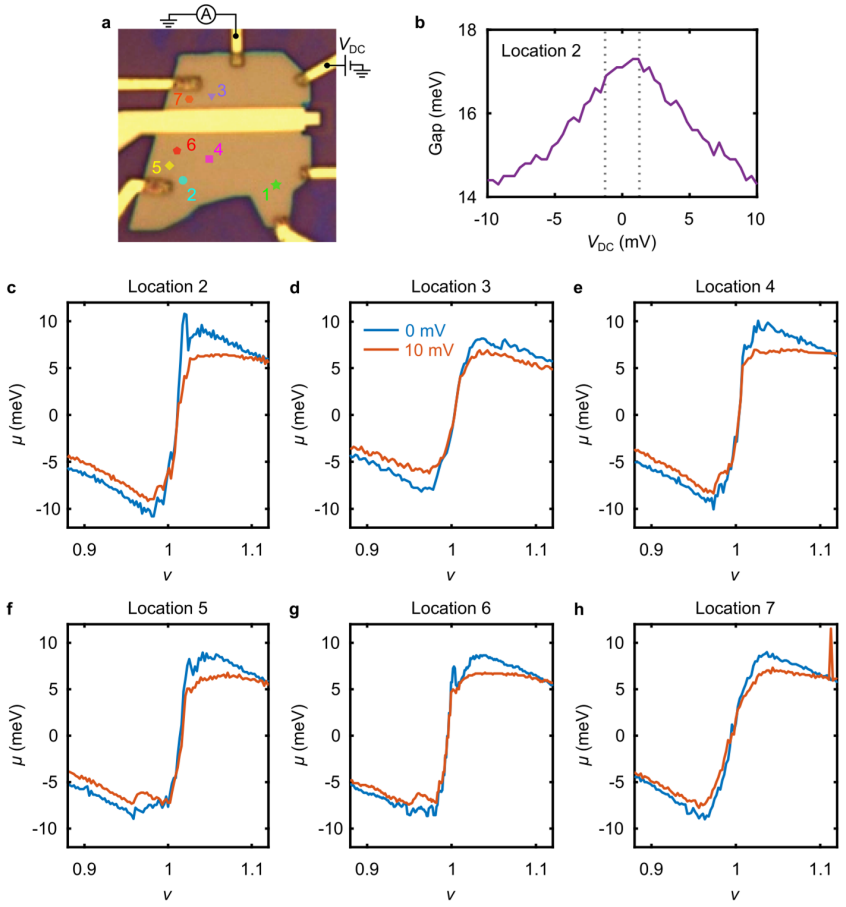

Extended Data Fig. 1 | Additional examples of the ν=1 gap suppression by the presence of magnons. a, Optical image of the device indicating the circuit used for magnon generation and the locations where the gap measurements were taken. **b**, Bias-dependent energy gap measured at location 2. The grey dotted lines mark $\pm E_Z$. While the origin of the small asymmetry for $|V_{DC}|<E_Z$ is unclear, its magnitude is much smaller than overall suppression observed at higher bias, and the top gate dependence shows that the onset consistently occurs near E_Z (see Fig. 2). **c-g**, Chemical potential μ near ν=1 measured with V_{DC}=0 mV (blue) and V_{DC}=10 mV (red) at 6 different locations. Although the local value of the ν=1 gap varies, its reduction by the presence of magnons is clearly reproduced in all the data sets.

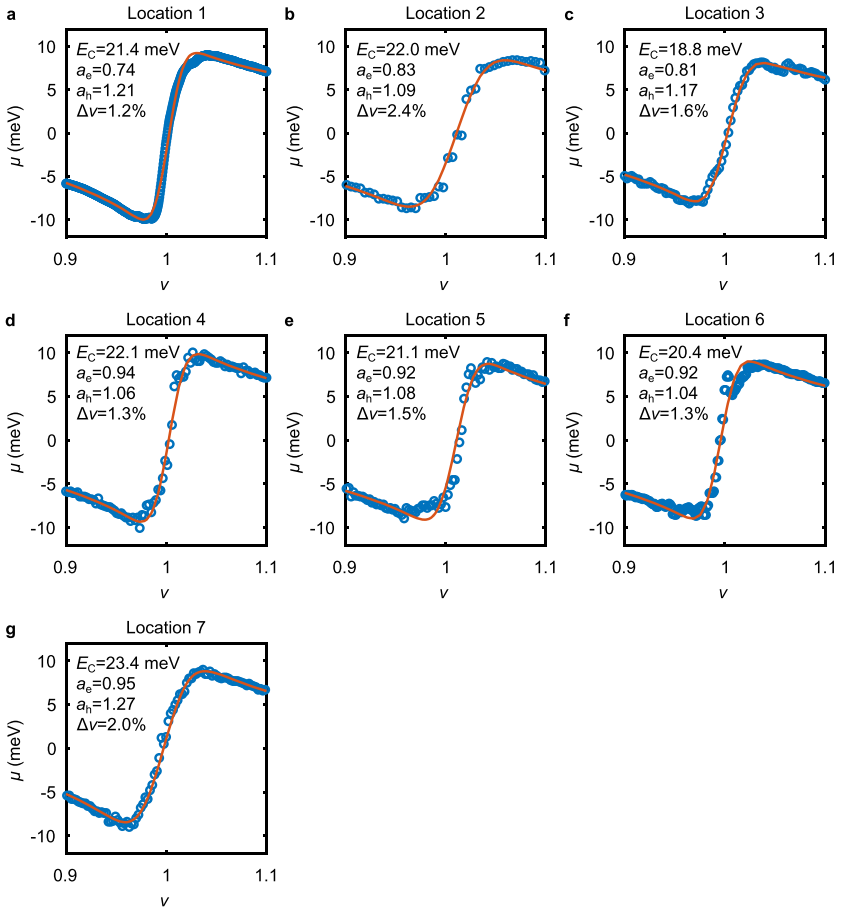

Extended Data Fig. 2 | Fitting of the chemical potential in the absence of magnons. a-g, Chemical potential μ near $\nu = 1$ measured with 0 mV (blue circles) DC bias applied to contact 3 and the best fit (red curves) using the skyrmion model by setting $\mu_m = 0$ meV (see Methods) at 7 different locations. The values of E_C obtained at these positions correspond to effective dielectric constants ε ranging from 10.0 to 12.4.

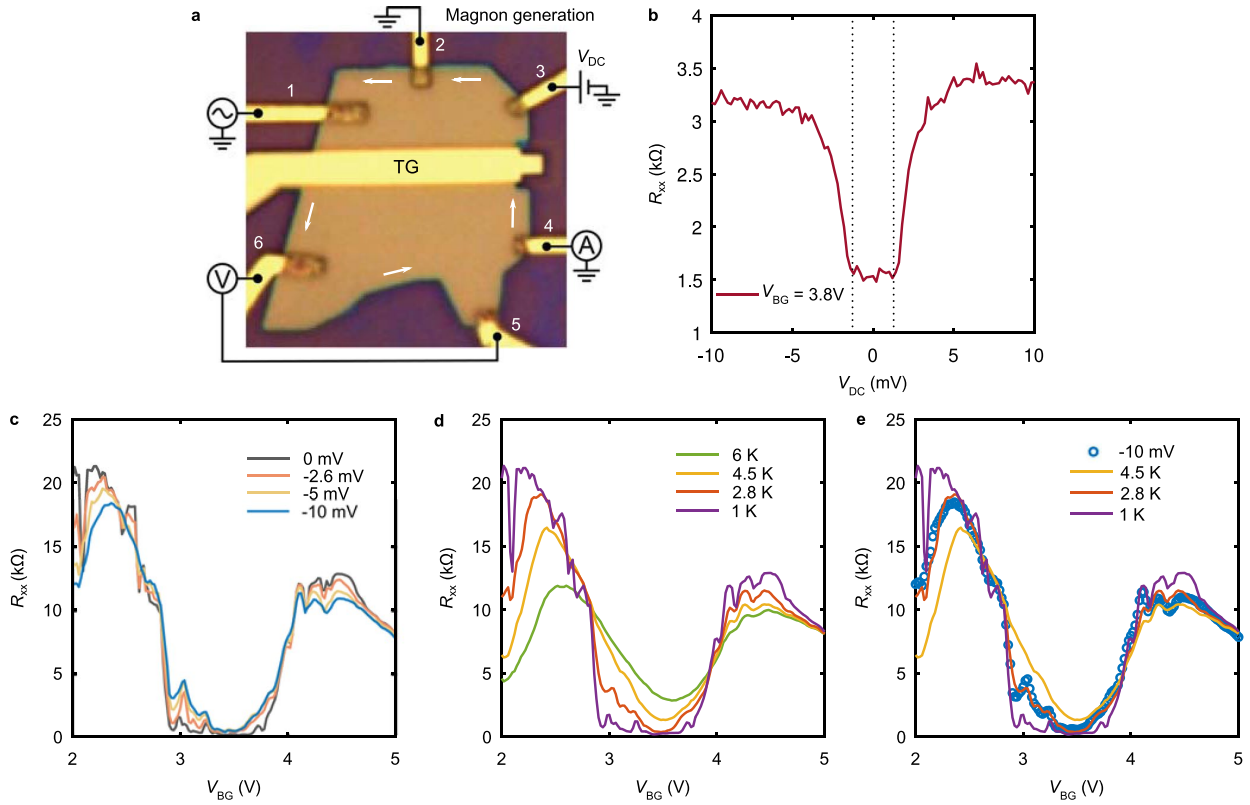

Extended Data Fig. 3 | R_{xx} thermometry. a, Circuit used for R_{xx} measurements. Contacts 2 and 3 are used to generate magnons. Contacts 1, 6, 5, and 4 are used to measure R_{xx}. The white arrows indicate the chirality of the current flow. **b**, R_{xx} as a function of V_{DC} at V_{BG} = 3.8 V. The value of R_{xx} tends to saturate for $|V_{DC}|$ greater than ~$4E_Z$, suggesting that the temperature saturates. **c**, Individual R_{xx} traces measured at base temperature with various values of V_{DC} applied to contact 3 near ν=1 using the circuit shown in **a**. The center of the ν=1 plateau is around a back gate voltage of 3.5 V. **d**, Individual R_{xx} traces measured at various temperatures with zero DC bias applied to contact 3 near ν=1 using the circuit shown in **a**. **e**, Individual R_{xx} traces measured at base temperature with 10 mV applied to contact 3 (blue dots) and at various temperatures with 0 mV applied to contact 3 (orange, yellow and purple lines). The close agreement between the blue dotted line and the red line suggests that the effect of magnon generation on the R_{xx} measurement is primarily due to heating. These measurements also demonstrate that the increase in temperature due to magnon generation does not exceed 4.5 K at V_{DC} = -10 mV.

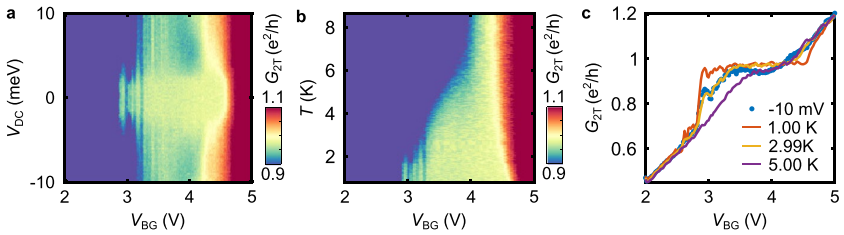

Extended Data Fig. 4 | Alternative derivation of electron temperature using two-terminal conductance G_{2T}. a, Bias-dependent two-terminal conductance G_{2T} measured in the vicinity of the $\nu=1$ plateau. **b**, Temperature-dependent G_{2T} measured at zero bias in the same range of electron densities. **c**, G_{2T} measured at -10 mV DC bias compared with selected zero-bias traces at elevated temperature.

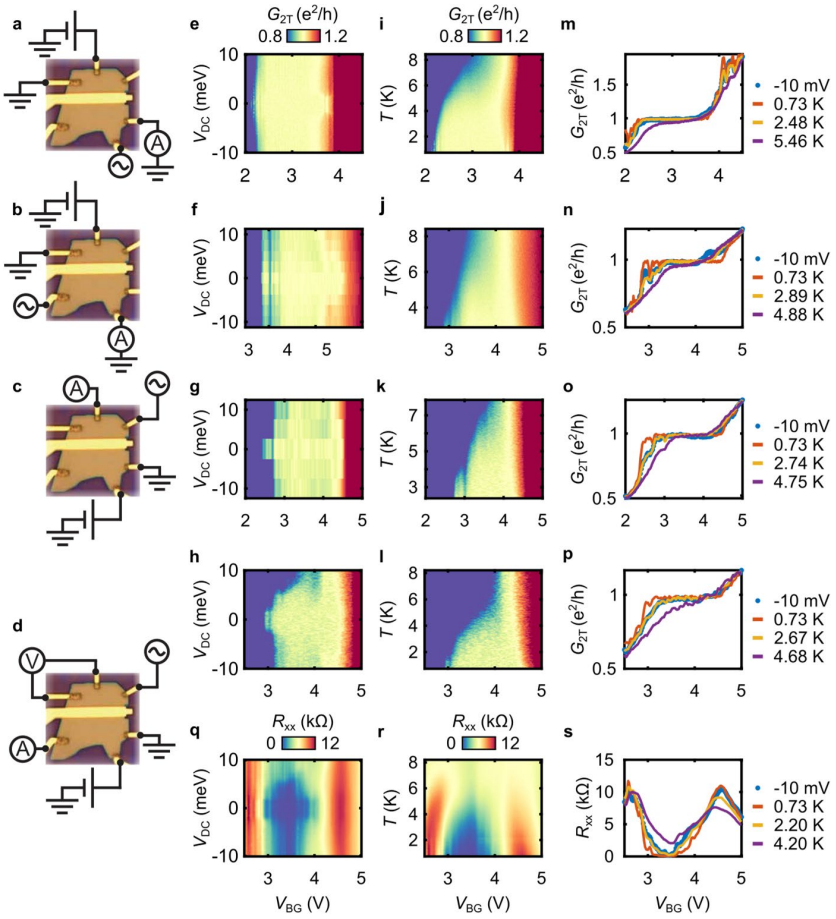

Extended Data Fig. 5 | Temperature extraction from additional circuit configurations. a-d, circuit configurations in which additional bias-dependent **(e-h)** and temperature dependent **(i-l)** two-terminal transport measurements were carried out. **m-p**, comparison of traces taken at V_{DC} = -10 mV and at base temperature with zero-bias traces taken at various temperatures. In each panel the middle value of temperature is that found to agree best with the V_{DC} = -10 mV trace in the least-squares sense. The good agreement between the -10 mV trace and the best-fit zero-bias trace indicates that the main effect of the bias in this circuit configuration is to elevate the temperature. **q-s**, additional R_{xx} data acquired simultaneously with G_{2T} using the circuit configuration shown in **d**. Estimation from R_{xx} gives a slightly lower temperature than G_{2T}.

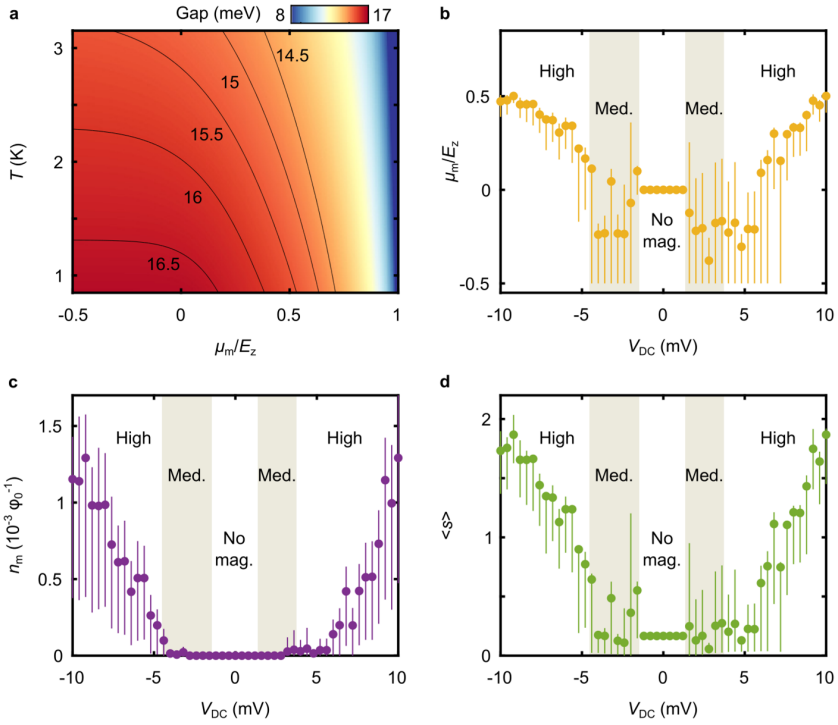

Extended Data Fig. 6 | Thermodynamics of free and bound magnons extracted from location 2. a, ν=1 gap as a function of magnon chemical potential μ_m/E_z and temperature T computed using the skyrmion model. **b-d**, Magnon chemical potential μ_m/E_z (**b**), free magnon density per flux n_m (**c**) and the mean number $<s>$ of extra flipped spins carried by a charge (**d**), extracted from the skyrmion model (see Methods). The shaded region corresponds to a medium bias regime where heating due to magnon injected plays a key role.

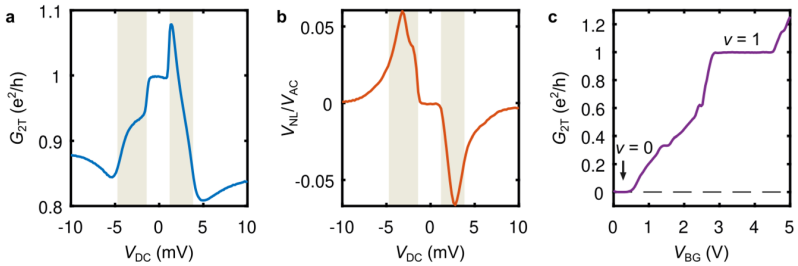

Extended Data Fig. 7 | Three regimes in magnon transport characteristics. a, G_{2T} averaged over values of V_{BG} on the ν=1 plateau as a function of DC bias. **b**, V_{NL}/V_{AC} averaged over values of ν_{TG} for $0 < \nu_{TG} < 2$. On each plot, the low-, medium- and high-bias regimes are indicated by shading in the same manner as Fig. 3. **c**, zero-bias measurement of G_{2T} showing a well-developed $\nu = 0$ plateau, implying an insulating $\nu = 0$ ground state as observed in previous transport studies of magnon generation.

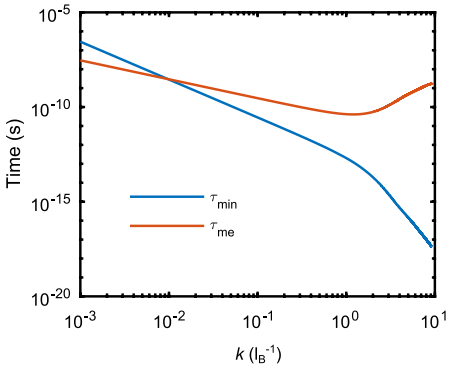

Extended Data Fig. 8 | Magnon lifetime and electron-magnon scattering time. Magnon lifetime and magnon-electron scattering time as a function of momentum, showing that only for very small momenta $k \lesssim 0.01 l_B^{-1}$ is $\tau_{min}(k)$ expected to exceed $\tau_{me}(k)$. Thus, all magnons with $k \gtrsim 0.01 l_B^{-1}$ are expected to be well-thermalized with the skyrmion population at temperature T.

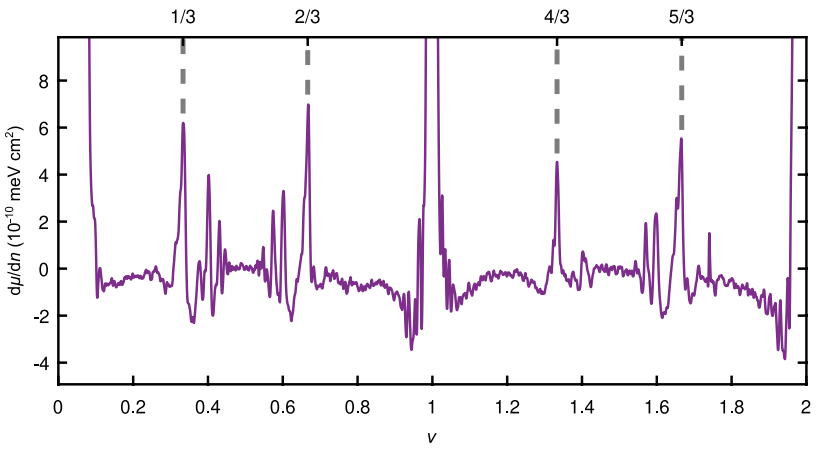

Extended Data Fig. 9 | Robust $\nu = 5/3$ state. Local inverse compressibility $d\mu/dn$ measured for $0 < \nu < 2$. In contrast to local compressibility studies performed on suspended monolayer graphene devices, a prominent peak at $\nu = 5/3$—comparable in strength to those at 1/3 and 2/3, and stronger than that at 4/3—is evident, suggesting that valley skyrmion formation in the device is *disfavored*.

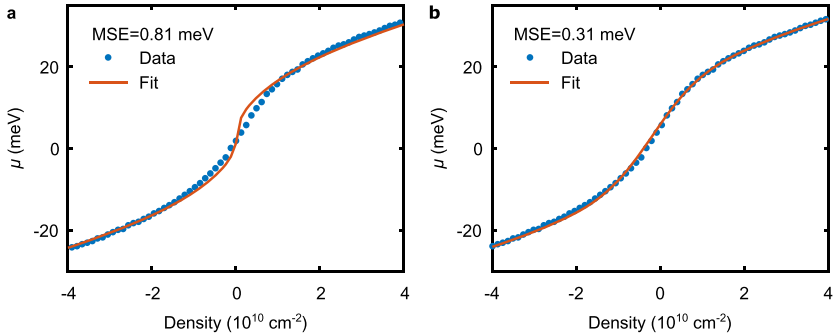

Extended Data Fig. 10 | Zero-field fits to the Dirac point. a, Fit comparing measured data to a model with no disorder broadening. The fit favors zero sublattice gap. **b**, Fit comparing measured data to a model with disorder broadening. The fit favors a scenario with a 12.3 meV sublattice gap with a disorder-broadening parameter of approximately 7×10^9 cm^{-2}, similar in magnitude to the broadening inferred from high-field compressibility measurements. The mean squared error (MSE) of the broadened fit is improved compared to that of the unbroadened fit by more than a factor of two.